# Superglass formation in an atomic BEC with competing long-range interactions

Stefan Ostermann <sup>©</sup>, <sup>1,\*</sup> Valentin Walther, <sup>1,2</sup> and Susanne F. Yelin <sup>1</sup> Department of Physics, Harvard University, Cambridge, Massachusetts 02138, USA <sup>2</sup>ITAMP, Harvard-Smithsonian Center for Astrophysics, Cambridge, Massachusetts 02138, USA

(Received 30 September 2021; accepted 7 April 2022; published 27 April 2022)

The complex dynamical phases of quantum systems are dictated by atomic interactions that usually evoke an emergent periodic order. Here, we study a quantum many-body system with two competing and substantially different long-range interaction potentials where the dynamical instability towards density order can give way to a disordered amorphous solid, which exhibits local density modulations but no long-range periodic order. We consider a two-dimensional Bose-Einstein condensate in the Rydberg-dressing regime coupled to an optical standing wave resonator. The dynamic pattern formation in this system is governed by the competition between the two involved interaction potentials: repulsive soft-core interactions arising due to Rydberg dressing and infinite-range sign changing interactions induced by the cavity photons. The amorphous phase is found when the two interaction potentials introduce incommensurate length scales. The dynamic formation of this peculiar phase can be attributed to frustration induced by the two competing interaction energies and length scales.

DOI: 10.1103/PhysRevResearch.4.023074

#### I. INTRODUCTION

The controllability of individual atomic systems increased tremendously over the past decades [1–6]. This enables efficient trapping and cooling of atomic gases or individual atoms, controlling individual photons, and tailoring interactions between atoms and photons. One particularly challenging and active modern research direction in this realm is systems with tailored long-range interactions [7]. Prominent examples are, among others, dipolar Bose-Einstein condensates (BECs) [8–11], ultracold atomic gases in cavities [12–14], and individually trapped atoms with Rydberg interactions [15–17]. These systems allow for the study of artificial quantum matter in a well-controlled and tunable environment.

Over the last decade the focus of research was on investigating long-range interacting systems with crystalline properties, i.e., periodic systems with long-range order. In this realm first experimental observations of quantum phase transitions like the superfluid to Mott insulator transition [18], the formation of supersolid phases of matter [19–26], or nontrivial spin phases [15,27,28] were realized and understood on a fundamental level. In recent years, the exploration of systems generating more complex patterns and phases became a leading research direction in many-body quantum physics. Particular focus hereby lies on quantum glasses [29–32], many-body localization [33,34], spin liquids [17,35]

Published by the American Physical Society under the terms of the Creative Commons Attribution 4.0 International license. Further distribution of this work must maintain attribution to the author(s) and the published article's title, journal citation, and DOI.

and quasicrystals [36–38]. Realizing such complex systems establishes a path towards a deeper understanding of interacting quantum many-body systems and provides insights on how different long-range interactions play together. Many of the effects mentioned above are related to frustration, i.e.,the inability to satisfy all constraints imposed by the competing long-range interactions. In this paper we introduce and study a particularly clean and experimentally well-controlled system which can give rise to frustration: a Rydberg-dressed BEC of neutral atoms trapped in an optical standing wave resonator [see Fig. 1(a)]. We elucidate some of the archetypal effects of the contest among the cavity-induced infinite-range interactions and long-range van der Waals (VdW) interactions among Rydberg atoms and ultimately leading to glassy behavior. Previous work that combined Rydberg atoms and cavities focused on either generating large optical nonlinearities for single photons [39-41] or spin models on a lattice where the motional degrees of freedom are frozen [29,41,42]. Here, we focus on the spatial dynamics and resulting density self-ordering of the gas under competing long- and infinite-range interactions. Both interaction potentials considered in this paper exhibit a self-ordering phase transition due to roton mode softening [43,44]. These soft roton modes are a direct result of the respective long-range interactions. However, the two types of interactions have substantially different properties. The Rydberg dressing results in spherically symmetric long-range soft-core interactions [see Fig. 1(b)] and the cavity photons induce anisotropic infinite-range periodic interactions between atoms [see Fig. 1(c)]. This distinguishes our paper from related studies focusing on a spherically symmetric interaction potential imposing two different length scales [45-47]. In fact, while these works use a synthetic theoretically motivated long-range interaction potential, our paper is based on an experimentally realistic configuration leading to the nontrivial physics presented below.

 $<sup>^*</sup>$ stefanostermann@g.harvard.edu

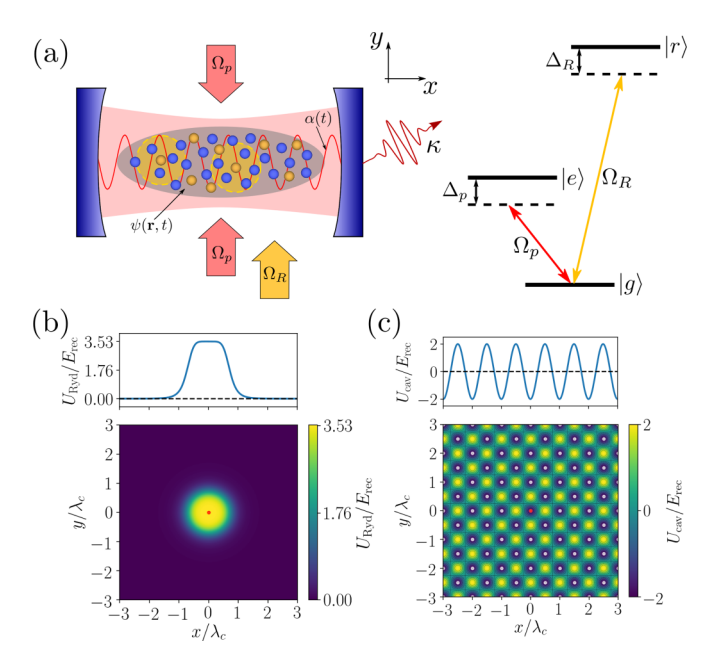


FIG. 1. (a) Considered setup. A Rydberg-dressed BEC is trapped and confined to two dimensions in an optical resonator with lasers impinging from the side. The BEC atoms form an effective V-level structure. The transition  $|g\rangle\leftrightarrow|e\rangle$  is coupled to the cavity at a strength  $\mathcal{G}_p$ . The transition  $|g\rangle\leftrightarrow|r\rangle$  is driven by an additional laser in the Rydberg dressing regime, implying that the high-lying Rydberg state  $|r\rangle$  is only very weakly populated. (b) The Rydberg dressing imposes a long-range soft-core interaction potential between the atoms. (c) In addition, the cavity photons induce nontrivial infinite range interactions between atoms. The top curves in panels (b) and (c) show cuts along the x axis at  $y = 0.0\lambda_c$  for the two interaction potentials.

As we will show in the following, the particular properties of the light-matter coupled system, i.e., the competition between the two nontrivial interactions at different length scales and the nonlinear interaction between the cavity mode and the BEC, lead to the dynamic formation of intriguing phases of quantum matter. In particular, we show how this system can be used to realize a stable glass phase, i.e., an amorphous solid with no long-range density order. The formation of this intriguing phase of quantum matter is attributed to geometrical frustration induced by the two competing interaction length scales and energies. In general the BEC also exhibits superfluidity and the resultant glassy phase is often also referred to as a superglass [30,48–51]. The formation of this disordered glassy state in our system is not triggered by an externally imposed disorder or an external lattice geometry which results in frustration. It is the interplay and particular nature of the two parts of the considered model (cavity photons in combination with van der Waals interactions) which gives rise to the phases presented below.

## II. MODEL

We consider a pancake-shaped BEC of N atoms confined in two dimensions and trapped inside an optical standing-wave resonator [see Fig. 1(a)]. The BEC atoms' ground state  $|g\rangle$  is coupled via the cavity to a low-lying excited state  $|e\rangle$  and,

simultaneously, to a highly excited Rydberg s state  $|r\rangle$ , realizing the V configuration illustrated in Fig. 1(a). The BEC atoms are pumped with a laser of frequency  $\omega_p$  impinging from the side, transverse to the cavity axis, which drives the transition  $|g\rangle \leftrightarrow |e\rangle$  at a Rabi frequency  $\Omega_p$ . This transition couples to a single cavity mode with a coupling strength  $\mathcal{G}_p$ . We consider the dispersive regime implying that the detuning  $\Delta_p =$  $\omega_p - \omega_{ge}$  is large compared to the Rabi frequency  $\Omega_p$  ( $\omega_{ge}$  is the transition frequency between  $|g\rangle$  and  $|e\rangle$ ). The transition  $|g\rangle \leftrightarrow |r\rangle$  is driven by an additional laser (with frequency  $\omega_R$ ) at a Rabi frequency  $\Omega_R$  in the Rydberg dressing regime implying a large detuning  $\Delta_R \gg \Omega_R$  with  $\Delta_R := \omega_R - \omega_{gr}$  ( $\omega_{gr}$  is the transition frequency between  $|g\rangle$  and  $|r\rangle$ ). This allows the adiabatic elimination of the Rydberg state  $|r\rangle$  resulting in an effective long-range two-body interaction potential [52–56], which is valid for sufficiently small atomic densities,

$$U_{\text{Ryd}}(\mathbf{r}, \mathbf{r}') = \frac{\tilde{C}_6}{R_c^6 + |\mathbf{r} - \mathbf{r}'|^6},\tag{1}$$

and arises due to the strong VdW interactions  $\propto C_6/|\mathbf{r}|^6$  ( $\mathbf{r} \in \mathbb{R}^2$ ) between Rydberg atoms. The parameters in Eq. (1) are defined as  $\tilde{C}_6 := (\frac{\Omega_R}{2\Delta_R})^4 C_6$  and  $R_c := (-\frac{C_6}{2\hbar\Delta_R})^{1/6}$ . An exemplary plot of the functional dependence of this long-range interaction potential is shown in Fig. 1(b). It was shown in previous work that a mean-field treatment suffices to capture the main features of cavity self-ordering [12,13,57] and Rydberg crystallization induced by the long-range interaction potential given in Eq. (1) [43,54,58]. Therefore, we focus on a mean-field treatment. Here, we present the most important equations used throughout this paper. A more detailed discussion of the model can be found in Appendix A. The dynamics is governed by two coupled equations. The equation for the BEC order parameter  $\psi(\mathbf{r}, t)$  is given as

$$i\hbar\partial_t \psi(\mathbf{r}, t) = \left[ -\frac{\hbar^2 \nabla^2}{2m} + \hbar U_0 |\alpha(t)|^2 \cos^2(k_c x) + 2\hbar \eta \operatorname{Re}[\alpha(t)] \cos(k_c x) \cos(k_c y) + \int_V d\mathbf{r}' U_{\operatorname{Ryd}}(\mathbf{r}, \mathbf{r}') |\psi(\mathbf{r}', t)|^2 \right] \psi(\mathbf{r}, t), \quad (2a)$$

and the dynamics of the mean-field cavity mode amplitude  $\alpha(t)$  is governed by

$$i\partial_t \alpha(t) = \{ -\Delta_c + U_0 B[\psi] - i\kappa \} \alpha(t) + \eta \theta[\psi]. \tag{2b}$$

In Eq. (2b) we introduced the cavity bunching parameter  $B[\psi] := \int_V d\mathbf{r} |\psi(\mathbf{r},t)|^2 \cos^2(k_c x)$  and the cavity mode order parameter  $\theta[\psi] := \int_V d\mathbf{r} |\psi(\mathbf{r},t)|^2 \cos(k_c x) \cos(k_c y)$ . The latter is the crucial quantity for understanding the self-ordering phase transition since the cavity mode can only take nonzero values if  $\theta[\psi] \neq 0$ , whereas the former only accounts for a cavity resonance frequency shift due to the BEC density. The potential depth of the cavity potential generated by intercavity photon scattering is defined as  $U_0 := \mathcal{G}_p^2/\Delta_p$ , and the effective pump strength is  $\eta := \Omega_p \mathcal{G}_p/\Delta_p$  in Eq. (2a). In addition,  $k_c = 2\pi/\lambda_c$  denotes the cavity wave number where  $\lambda_c$  is the cavity resonance wavelength. We also introduced the detuning of the pump laser frequency  $\omega_p$  with respect to the cavity resonance frequency  $\omega_c$  as  $\Delta_c := \omega_p - \omega_c$  and the cavity decay rate  $\kappa$ .

A particularly simple and insightful model can be obtained in the low-energy regime by adiabatically eliminating the cavity mode (for details, see Appendix A), which results in a new effective equation for the BEC dynamics:

$$i\hbar\partial_t \psi(\mathbf{r},t) = \left[ -\frac{\hbar^2}{2m} \nabla^2 + \int_V d\mathbf{r}' [U_{\text{cav}}(\mathbf{r},\mathbf{r}') + U_{\text{Ryd}}(\mathbf{r},\mathbf{r}')] |\psi(\mathbf{r}',t)|^2 \right] \psi(\mathbf{r},t).$$
(3)

Note that eliminating the cavity mode dynamics is only justified if the mode evolves on a much faster time scale than the center of mass motion of the atoms. In Eq. (3) we introduced the cavity two-body interaction potential induced by the cavity photons as

$$U_{\text{cav}}(\mathbf{r}, \mathbf{r}') = \hbar \mathcal{I} \cos(k_c x) \cos(k_c x') \cos(k_c y) \cos(k_c y'), \quad (4)$$

where  $\mathcal{I} := \eta^2(\Delta_c - NU_0/2)/[(\Delta_c - NU_0/2)^2 + \kappa^2]$  is the effective interaction strength. An exemplary plot of this infinite-range interaction potential is shown in Fig. 1(d). It is the competition between the two significantly different types of long-range interaction potentials  $U_{\rm Ryd}$  and  $U_{\rm cav}$  shown in Figs. 1(b) and 1(c) which contributes to the nontrivial emergent phases presented below. Note that the simplified model given in Eq. (3) provides a good intuitive picture about the fundamental interactions induced by the two model constituents. However, this approximate model does not cover all features arising from the nonlinear coupled dynamics of the cavity mode and the BEC [see Eq. (2)], as discussed below.

### III. ROTON INSTABILITIES

Roton-induced instabilities were first introduced and studied for superfluid helium-4 [59] but they are a common feature of systems with long-range interactions. A dynamical instability of a certain nonzero k mode in the collective excitation spectrum usually results in a phase transition from homogeneous to periodic order. The Bogoliubov excitation spectrum for plane-wave excitations on top of a homogeneous condensate for a system with two-body long-range interaction potentials reads [60]

$$\varepsilon(\mathbf{k}) = \sqrt{\frac{\hbar^2 \mathbf{k}^2}{2m} \left\{ \frac{\hbar^2 \mathbf{k}^2}{2m} + 2[U_{\text{Ryd}}(\mathbf{k}) + U_{\text{cav}}(\mathbf{k})] \right\}}, \quad (5)$$

where  $U_{\mathrm{Ryd}}(\mathbf{k})$  and  $U_{\mathrm{cav}}(\mathbf{k})$  denote the Fourier transforms (FTs) of the respective interaction potentials  $U_{\mathrm{Ryd}}(\mathbf{r},\mathbf{r}')$  and  $U_{\mathrm{cav}}(\mathbf{r},\mathbf{r}')$ . The FT of the Rydberg interaction potential cannot be expressed in a comprehensive analytical formula. The FT of the cavity interaction potential (4), however, is given as  $U_{\mathrm{cav}}(\mathbf{k}) = \hbar \mathcal{I} \sum_{i,j \in \{0,1\}} \delta_{k_x,(-1)^i k_c} \delta_{k_y,(-1)^j k_c}$ , where  $\delta_{k_1,k_2}$  denotes the Kronecker delta. In Fig. 2 an exemplary excitation spectrum is shown. The spherically symmetric Rydberg interaction potential induces roton softening along a circle with a radius  $k_{\mathrm{Ryd}}$  [indicated by the dashed orange line in Figs. 2(a) and 2(b)]. The cavity interaction potential, however, results in four  $\delta$ -shaped peaks/minima which are indicated by the white circles in Figs. 2(a) and 2(b), and are more prominently visible in panels Figs. 2(c) and 2(d). Hence, while the two interaction potentials considered in this paper both result in dynamical

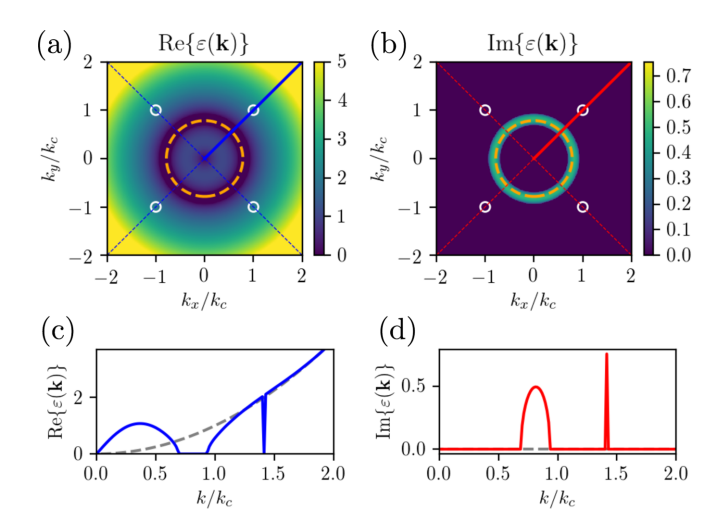


FIG. 2. Real and imaginary part of the excitation spectrum given in Eq. (5) for  $\tilde{C}_6=2.2E_{\rm rec}$  and  $\eta=1.1\eta_{\rm crit}$ , i.e.,both interaction strengths above the threshold condition. The dashed orange circle in panels (a) and (b) marks the roton minimum induced by the spherically symmetric Rydberg interaction. The white circles indicate the four  $\delta$ -like rotons generated by the cavity interaction potential. Panels (c) and (d) show a cut along the diagonals for positive  $k_x$  and  $k_y$  values [red and blue lines in panels (a) and (b)]. The other parameters are  $R_c=0.92\lambda_c$ ,  $\Delta_c=-10.0\omega_{\rm rec}$ ,  $\kappa=5.0\omega_{\rm rec}$ , and  $U_0=-1.0\omega_{\rm rec}$ .

instabilities induced by roton mode softening, the properties of the related excitation spectra differ significantly. The cavity roton positions are always fixed by the cavity wavelength and are located at a value  $k_{\rm cav} \coloneqq \sqrt{2}k_c$  while the value of  $k_{\rm Ryd}$  can be tuned via the parameter  $R_c$  in Eq. (1). Since each unstable k mode can be associated with a characteristic length scale via  $k_{\rm Ryd} = 2\pi/l_{\rm Ryd}$  and  $2\pi/l_{\rm cav}$ , the role of different emergent length scales on the final steady or ground state can be analyzed by changing  $R_c$  correspondingly. This can either be achieved by dressing to a different Rydberg state ( $\tilde{C}_6$  scales like  $n^{11}$ , where n is the principal quantum number) or by changing the detuning  $\Delta_R$ .

The homogeneous solution gets unstable toward a periodically ordered pattern if the excitation spectrum acquires an imaginary part at a nonzero  $\mathbf{k}$  value, i.e.,min $\{\text{Re}[\varepsilon(\mathbf{k})]|_{|\mathbf{k}|>0}\}=0$ . This results in two critical values  $\tilde{C}_6^{\text{crit}}$  (critical Rydberg interaction strength) and  $\eta_{\text{crit}}$  (critical effective cavity pump strength). Since the FT of the cavity interaction potential is solely given as the sum of four Kronecker-delta functions it is possible to find an analytical expression for the threshold for the pure cavity self-ordering case. Setting  $\tilde{C}_6$  to zero and applying the threshold condition for  $k=k_{\text{cav}}$  in Eq. (5) results in

$$\eta_{\text{crit}} = \sqrt{\frac{(\Delta_c - NU_0/2)^2 + \kappa^2}{NU_0 - 2\Delta_c}} 2\sqrt{\omega_{\text{rec}}},\tag{6}$$

which is the known threshold for self-organization of a BEC in a cavity in two dimensions [13].

These insights yield a first intuitive phase diagram shown in Fig. 3. We expect the phase diagram to exhibit four different regions. In each region either none, one, or two of the respective rotons are unstable (indicated by red circles

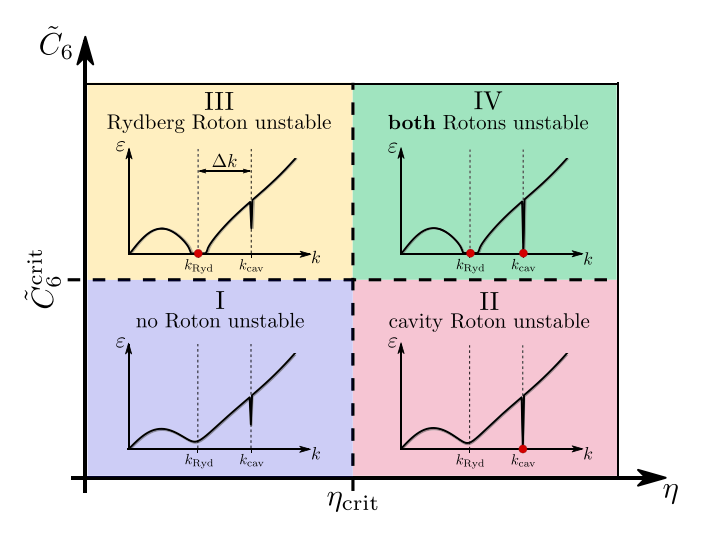


FIG. 3. Sketch of the expected phase diagram based on the excitation spectrum. We distinguish four regions: I, no roton softened, i.e.,the homogeneous solution is stable; II, the cavity roton touches zero (indicated by red circle), i.e.,acquires an imaginary part; III, the Rydberg roton is unstable at  $k = k_{\rm Ryd}$ ; IV, both rotons are unstable. The distance  $\Delta k$  between the two k values at which the rotons soften can be tuned by tuning  $R_c$  in Eq. (1).

in Fig. 3). In addition to the two interaction strengths tuned in the phase diagram, the system features another relevant free parameter—the Rydberg interaction range  $R_c$ . In the following we will restrict ourselves to three cases: (i)  $k_{Ryd} =$  $k_{\text{cav}}$  which is obtained by choosing  $R_c = 0.51\lambda_c$ , (ii)  $k_{\text{Ryd}} =$  $k_{\rm cav}/\sqrt{2} = k_c$  with  $R_c = 0.72\lambda_c$ , and (iii)  $k_{\rm Ryd} = k_{\rm cav}/2$  with  $R_c = 1.2\lambda_c$ . A sketch of the unstable roton length scales in k space for all three cases is shown in Fig. 4. We restrict ourselves to cases where  $k_{Ryd} < k_{cav}$  because only in this case the additional Rydberg length scale competes with the length scale set by the cavity potential (see also Appendix B). Note that the first two cases (i) and (ii) are special cases because the two wave numbers are either the same [case (i)] or  $k_{Rvd}$  is commensurate with  $k_c$ , i.e., the fundamental length scale along the cavity axis [case (ii)]. Case (iii), however, corresponds to one example of the most general incommensurate scenario. We chose a factor 2 for the wave-number ratio in case (iii) but

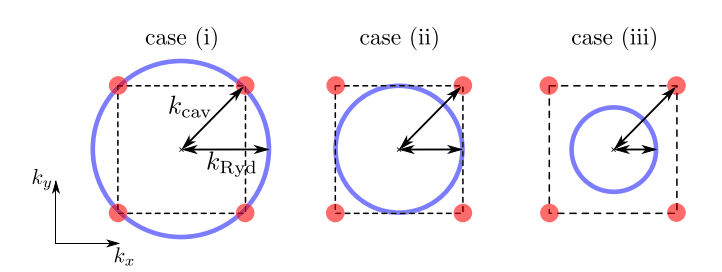


FIG. 4. The three cases considered in this paper. The red dots mark the four k modes which are unstable due to the cavity interaction potential (see Fig. 2). The blue circle indicates all k values which are unstable due to the Rydberg dressing potential: case (i),  $k_{\rm Ryd} = k_{\rm cav}$ ; case (ii),  $k_{\rm Ryd} = k_{\rm cav}/\sqrt{2} = k_c$ ; case (iii),  $k_{\rm Ryd} = k_{\rm cav}/2$ . The cases (i) and (ii) represent special cases, whereas case (iii) corresponds to one example for the most general scenario.

the same qualitative results as presented below were obtained for a variety of different wave-number ratios.

#### IV. SELF-CONSISTENT GROUND STATE

One major element of the studied system is the interplay between the dynamic cavity field and the BEC dynamics. While the simplified model given in Eq. (3) provides a good intuitive picture about the features and roles of the two different interactions, it does not fully capture the competing time scales in the system. Hence, we now analyze the full system given in Eq. (2). We calculate the self-consistent ground state for the set of Eqs. (2) via a variational approach. To this end, we employ a self-consistent iterative algorithm.

- (1) Choose a random initial steady-state value  $\alpha_{SS}$ .
- (2) Plug this value into the Gross-Pitaevskii equation (GPE) (2a) and perform an imaginary time evolution  $(t \rightarrow -i\tau)$  to find the lowest-energy state.
- (3) Calculate a new steady state of Eq. (2b) by setting  $\partial_t \alpha(t) = 0$  and solving for  $\alpha$ .

We iterate until we find a state where  $|\alpha_{SS}|$  lies within a convergence radius of  $10^{-6}$ . All numerical simulations for the remainder of this paper are performed for  $x, y \in [-10\lambda_c, 10\lambda_c]$  with periodic boundary conditions. Note that this self-consistent algorithm is not necessarily convex. In general, the energy functional

$$\mathcal{E}[\psi] = \int_{V} d\mathbf{r} \left[ -\frac{\hbar^{2} \nabla^{2}}{2m} + \hbar U_{0} |\alpha(t)|^{2} \cos^{2}(k_{c}x) + 2\hbar \eta \operatorname{Re}[\alpha(t)] \cos(k_{c}x) \cos(k_{c}y) + \int_{V} d\mathbf{r}' U_{\operatorname{Ryd}}(\mathbf{r}, \mathbf{r}') |\psi(\mathbf{r}')|^{2} \right] |\psi(\mathbf{r})|^{2},$$
(7)

which results in the GPE (2a), can have multiple local minima for a given value of  $\alpha$ . Whether one finds the global minimum or not depends on the initial condition for the imaginary time evolution. Therefore, we perform this algorithm for various different initial conditions and compare the obtained values of  $|\alpha|$  and the corresponding ground-state energies by evaluating the energy functional in Eq. (7). We focus on seven particular initial conditions throughout this paper. They are generated by superimposing localized Gaussian wave functions  $\phi_{\sigma}(\mathbf{r}) = C \exp[-|\mathbf{r}|^2/(2\sigma^2)]$  with a certain width  $\sigma$  to generate a BEC wave function  $\psi(\mathbf{r}) = \sum_i \phi_{\sigma}(\mathbf{r} - \mathbf{R}_i)$  with a certain spatial density distribution determined by the positions  $\mathbf{R}_{i}$ . The seven initial conditions are a homogeneous density (hom), a checkerboard lattice (CB), a period doubled CB lattice (PD CB), a hexagonally closed packed lattice (hcp), a square lattice (square), and staggered chains rotated at  $\pi/4$ (RC 1) and  $3\pi/4$  (RC 2). Details on the individual initial conditions can be found in Appendix B and the density distributions of all nontrivial initial conditions are shown in Fig. 10. Only if all initial conditions result in the same energy and mode amplitude the energy minimization problem is convex.

## A. Case (i): Equal length scales

We first consider the special case where  $k_{\rm Ryd} = k_{\rm cav}$  (see Fig. 4), which implies equal length scales  $l_{\rm Ryd} = l_{\rm cav}$ 

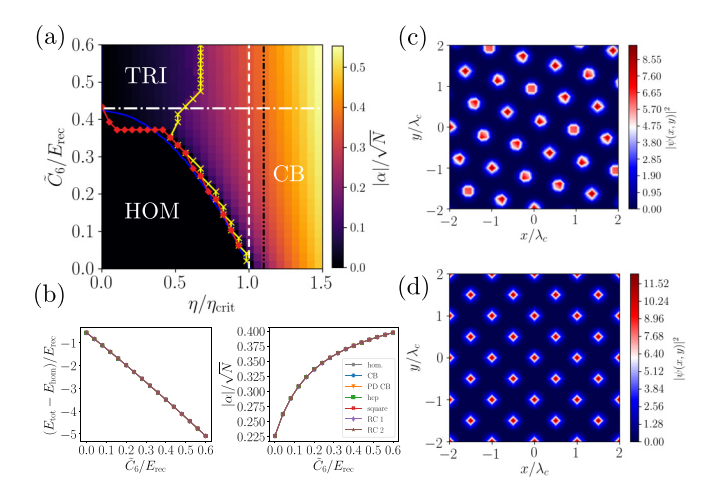


FIG. 5. (a) Self-consistent ground-state phase diagram for case (i):  $k_{\text{Ryd}} = k_{\text{cav}}$  ( $R_c = 0.51\lambda_c$ ). The white dashed and dash-dotted lines indicate the the critical values for independent Rydberg crystallization (horizontal white dash-dotted) or cavity self-organization (vertical white dashed). The blue curve is the critical value at which the excitation spectrum in Eq. (5) touches zero for the given parameters. The red curve with diamond markers indicates the transition line from homogeneous to periodic order. The yellow curve with x markers is the transition line between the different phases, i.e.,the line at which  $|\alpha|$  exhibits a kink. (b)  $|\alpha|$  values and ground-state energies (shifted by the energy of the homogeneous solution  $E_{hom}$ ) for values along the black dash-dot-dotted line in panel (a) for all seven initial conditions. (c) Exemplary density distribution for the triangular (TRI) lattice phase with  $\eta = 0.2\eta_{\rm crit}$  and  $\tilde{C}_6 = 0.6E_{\rm rec}$ . (d) Exemplary density distribution for the checkerboard (CB) lattice phase with  $\eta = 1.1 \eta_{\rm crit}$  and  $\tilde{C}_6 = 0.6 E_{\rm rec}$ . All other parameters as in Fig. 2.

 $(R_c = 0.51\lambda_c)$ . In this case, the regions II and IV in the phenomenological phase diagram in Fig. 3 are expected to merge. This is verified by the numerical phase diagram shown in Fig. 5(a). It exhibits three different phases: a homogeneous phase (HOM), a triangular phase (TRI) [see Fig. 5(c)], and a checkerboard lattice phase (CB) [see Fig. 5(d)]. We use two different quantities to obtain the phase boundaries from the numerically obtained data. First, we determine the line along which the cavity mode amplitude  $|\alpha|$  exhibits a kink, i.e.,an abrupt change in the gradient. This is a clear indication of a phase transition [vellow line with x markers in Fig. 5(a)]. Second, we obtain the transition line from homogeneous to periodic order by calculating the ground-state energy obtained from Eq. (7) and shifting it with respect to the energy of the homogeneous state  $E_{\text{hom}}$ , which is obtained by evaluating Eq. (7) for  $\alpha = 0.0$  and a homogeneous BEC density. Energies are given in units of the recoil energy  $E_{\rm rec} := \hbar^2 k_c^2/(2m) =$  $\hbar\omega_{\rm rec}$  throughout this paper. This quantity is zero if no periodic order emerges and nonzero elsewhere. This results in the red line with diamond markers in Fig. 5. The TRI state only forms for weak cavity pump strengths and for strong Rydberg interaction strengths. For increasing cavity pump, the system organizes in a checkerboard pattern, which is the configuration realized in cavity self-organization without Rydberg dressing [12,13]. Note, however, that the softening of the Rydberg roton affects the threshold for cavity selfordering as it can already be seen by the blue line in Fig. 5(a), which is obtained via the excitation spectrum in Eq. (5). This implies that the effect of the Rydberg roton can be observed already far below the critical Rydberg interaction strength  $\tilde{C}_6^{\rm crit}$ . This is a remarkable result as the observation of density modulation due to Rydberg dressing has proven elusive in experiments [56] due to experimental complications such as unfavorable scaling with the density and long time scales required for experiments. Our results suggest a way to observe effects of Rydberg dressing indirectly for much smaller Rydberg fractions (i.e., smaller  $\tilde{C}_6$ ). It should be remarked that there is a parameter regime  $(\eta/\eta_{crit} \in [0.0, 0.5])$  where the phase boundaries for the HOM  $\rightarrow$  TRI transition obtained via Eq. (5) only coincide with the numerically obtained ground state for  $\eta/\eta_{\rm crit} = 0.0$ . The deviations from the blue line for larger values of  $\eta$  can be attributed to the additional nonlinearity of the set of equations in Eq. (2), which is not covered by the simplified model used to determine Eq. (5). In Fig. 5(b) we show the obtained ground-state energy obtained from Eq. (7) and the cavity mode amplitude for all seven employed initial conditions. Again we shifted all energies with respect to the homogeneous state energy  $E_{\text{hom}}$ . We find that all curves for all initial conditions lie on top of each other, implying that this particular iterative energy minimization for case (i) is convex in  $\psi$  and  $\alpha$ . Note that in general the self-ordering phase transition HOM  $\rightarrow$  CB is known to break a discrete  $Z_2$ symmetry [61]. This symmetry breaking can also be observed in the study system; however, we restrict our discussion to one symmetry broken phase throughout this paper.

### B. Cases (ii) and (iii): Different length scales

The main property of the considered system is that two interactions with different functional dependence and different intrinsic length scale are combined. Here, we show that this feature results in highly nontrivial physics which goes beyond what is achievable with only a single model constituent. Figure 6 exhibits the two obtained ground-state phase diagrams together with the additional nontrivial density distributions realized in these regimes. Since now two fundamental length scales become unstable the phase diagram resembles the intuitive picture from Fig. 3 and contains four different phase regions. This results in additional phases—a square lattice (SQ) [for case(ii)] and a rotated chain (RC) phase [for case (iii)], respectively. The critical parameters for the phase transitions between the CB phase and these newly formed phases are indicated by the green line with circle markers in Figs. 6(a) and 6(b). At this transition the cavity mode exhibits a kink as it can be seen from Figs. 6(b) and 6(d). The other phase boundaries in panels (a) and (b) of Fig. 6 are obtained via the same method as it was outlined in the previous section. We find that now the critical values obtained via Eq. (5) in Sec. III, however, do not coincide with the numerical values at all. This again shows that the simplified model discussed in Sec. III for the adiabatically eliminated cavity dynamics [see Eq. (3)] provides a good first intuition about the contributing interactions and the expected phase diagram, but fails for different competing length scales due to a breakdown of the adiabatic solution. This is due to the influence of the additional Rydberg length scale on the mode dynamics which

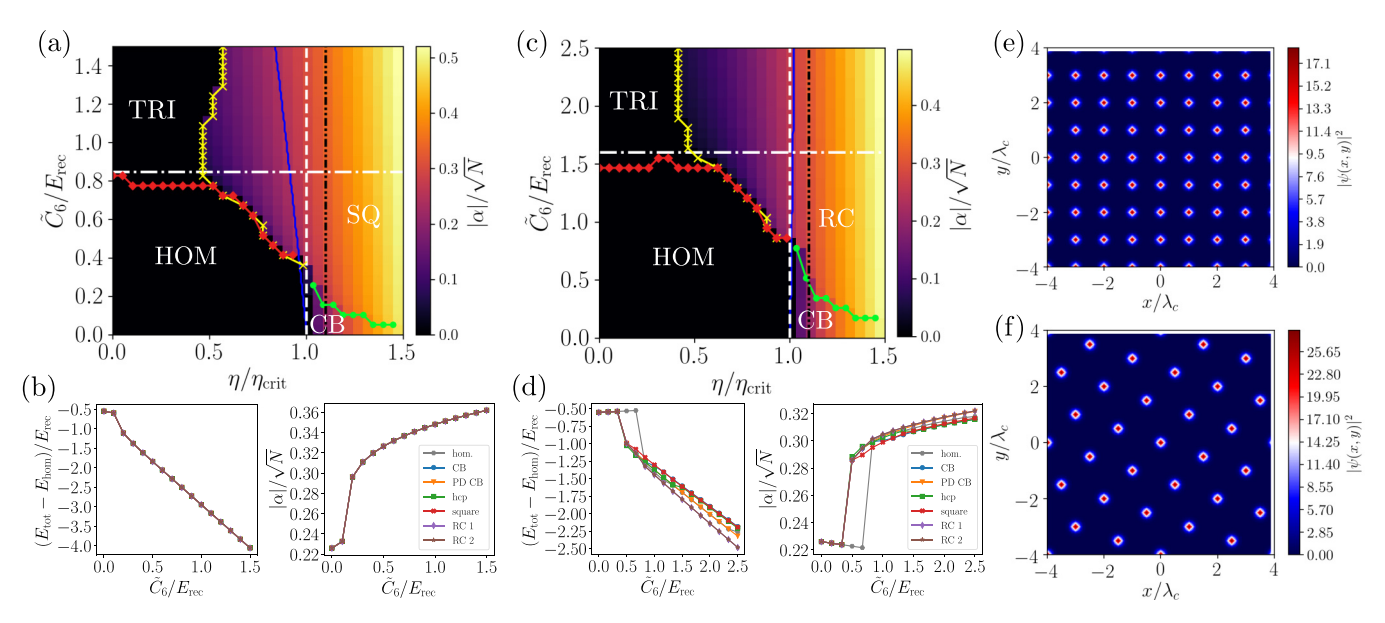


FIG. 6. (a) Numerical phase diagram for case (ii):  $k_{\rm Ryd} = k_{\rm cav}/\sqrt{2}$  ( $R_c = 0.72\lambda_c$ ). (b) Ground-state energy and cavity mode amplitude  $|\alpha|$  along the vertical black dash-dot-dotted line in panel (a) for all seven initial conditions. (c) Numerical phase diagram for case (iii):  $k_{\rm Ryd} = k_{\rm cav}/2$  ( $R_c = 1.2\lambda_c$ ). (d) Same as panel (b) but for case (iii). The different initial conditions no longer result in the same ground-state energies and mode amplitudes. The iterative energy minimization is not convex. The yellow and red lines indicating the phase boundaries in panels (a) and (c) are obtained as in Fig. 5(a). The green line indicates another phase transition between two ordered phases as it can also be seen from panels (b) and (d). (e) Exemplary ground-state density distribution for the square (SQ) phase for case (ii). (f) Exemplary ground-state density distribution for the rotated chain phase for case (iii). Note that the same density distribution rotated by  $\pi/2$  is a ground state as well, as the degeneracy between RC 1 and RC 2 in panel (d) indicates. All other parameters are the same as in Fig. 5(a).

is taken into account in the full numerics resulting in the phase diagrams shown in Fig. 6. The instability in this system is actually induced by the combined collective instability of the BEC density *and* the cavity mode amplitude. The fluctuations of the BEC couple to the fluctuations of the cavity mode and vice versa. This results in actual thresholds for the transitions TRI  $\leftrightarrow$  SQ and CB  $\leftrightarrow$  SQ in Fig. 6(a) and TRI  $\leftrightarrow$  RC and CB  $\leftrightarrow$  RC in Fig. 6(c) that are below the values anticipated by the simplified excitation spectrum in Eq. (5). This again could facilitate the experimental observation of effects induced due to Rydberg induced roton mode softening at smaller Rydberg interaction strengths  $\tilde{C}_6$ .

For case (ii) we find that, in addition to the TRI and CB phases, a SQ lattice phase emerges [see Fig. 6(e)]. This phase is a direct result of the nontrivial interplay between the two different interactions at these particular length scales. All seven initial conditions again result in the same ground-state energies and mode amplitudes [see Fig. 6(b)]. This feature changes in the incommensurate case (iii)— $k_{Rvd} = k_{cav}/2$ . We identify an additional RC phase [see Figs. 6(c) and 6(f)], where the iterative energy minimization in the self-consistent algorithm is no longer convex. There are two possible realizations of the RC phase. In Fig. 6(f), we show one possible realization. However, the given density pattern rotated by  $\pi/2$ is another ground state with the same energy. This can be seen by the two degenerate lowest-energy curves in Fig. 6(d) which correspond to the two possible realizations of the RC phase. The two degenerate states maximize the population of the cavity mode [see Fig. 6(d)] while fulfilling the length scale restrictions imposed by the Rydberg interactions (see Appendix B for details). Such degeneracy in combination with nonconvex features is a prime indicator for geometrical frustration ultimately leading to glassiness as we show in the next section. Note that we restricted our analysis on three cases for a concise presentation of the results. It should be mentioned that cases (i) and (ii) are indeed two special cases, which lead to a convex problem. Any other choice [case (iii) is one possibility] of length scale ratios results in a nonconvex energy landscape. The nonconvex nature of the energy landscape in case (iii) is the crucial feature which results in the dynamic formation of the superglass phase presented below.

## V. DYNAMICS

It is *a priori* unclear whether the self-consistent ground state can be reached by dynamically evolving Eq. (2) in real time. While this is usually the case for systems with a unique lowest-energy state, ground-state degeneracy in combination with higher-lying energy states may block the dynamical realization of the RC phase in case (iii). In fact, we will show below that the steady state for case (iii) is an amorphous solid with no long-range density order.

In Fig. 7, the time evolution of the cavity mode amplitude and the total energy together with the steady-state density distribution at  $t = 500/\omega_{\rm rec}$  is shown for case (ii). The time evolution is obtained by solving the full model given in Eq. (2) with initial conditions defined as a homogeneous, i.e., spatially constant, BEC order parameter  $\psi(\mathbf{r},t)$  with a tiny random seed on top, and an empty cavity mode  $\alpha(t=0)=0.0$  for the cavity mode. We find that the square lattice obtained in the previous section can be reached dynamically and that it renders a stable steady state. In contrast, the steady state

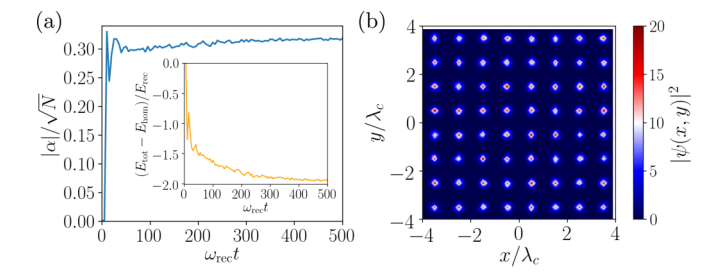


FIG. 7. (a) Time evolution of the cavity mode amplitude for case (ii). The inset shows the corresponding time evolution of the total energy obtained via Eq. (7). (b) Steady state at  $t = 500/\omega_{\rm rec}$ . Parameters:  $\eta = 1.1\eta_{\rm crit}$ ,  $\tilde{C}_6 = 1.0E_{\rm rec}$ ,  $R_c = 0.72\lambda_c$ . All other parameters as in Fig. 2.

for case (iii) is stable but not the rotated chain state as the self-consistent phase diagram suggests. The steady state is an inhomogeneous density pattern with local but no long-range density order. In Fig. 8(a), we show three outcomes for three independent runs of the time evolution for the same parameters. Every run results in a different density distribution. This feature, in addition to the BEC's superfluidity, qualifies this phase as a so-called superglass [48–50]. Note that the employed mean-field model assumes the gas to be superfluid for all parameter choices. In general, superfluidity can be lost for large cavity pump strength and/or Rydberg interaction. For the parameters used here even large values of  $\tilde{C}_6$  and  $\eta$ still allow some tunneling between different density peaks and, therefore, phase coherence between individual density peaks is expected to be maintained. The glassy behavior can be directly understood from the nonconvex properties and the degeneracy of the energies found in the previous section

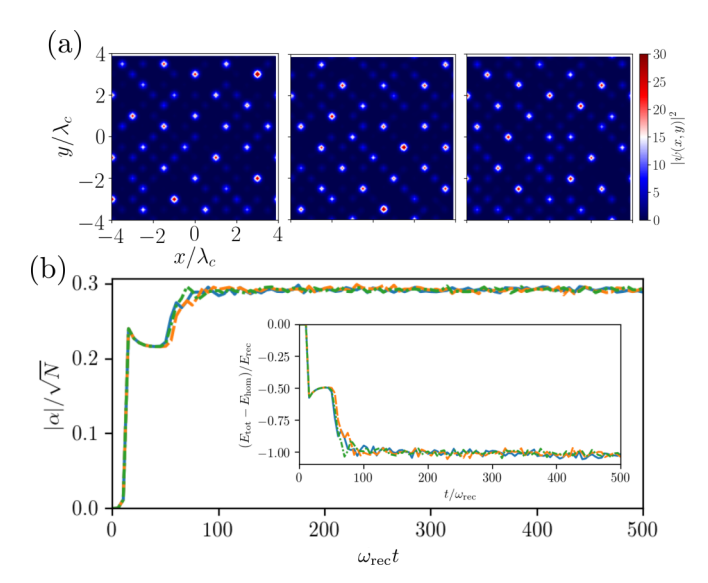


FIG. 8. (a) Three different steady states for three runs for case (iii). Each run generates a different density pattern with no long-range order. This is a typical indication of an amorphous solid (or a glass phase). All realized patterns, however, scatter exactly the same amount of light into the cavity as it can be seen from panel (b). Parameters:  $\eta = 1.1\eta_{\rm crit}$ ,  $\tilde{C}_6 = 1.5E_{\rm rec}$ ,  $R_c = 1.2\lambda_c$ . All other parameters as in Fig. 2.

[see Fig. 6(f)]. Each run results in a different mixture of the degenerate ground states giving rise to the glassy steady state. Remarkably, however, the resulting different density distributions still have exactly the same steady-state cavity mode amplitude. Hence, the different glassy states are not distinguishable via the cavity fields. Note that the formation of this superglass state is a direct consequence of the competition between the two particularly chosen interaction potentials and cannot be straightforwardly realized by combining *any* two long-range interaction potentials.

#### VI. CONCLUSIONS AND OUTLOOK

We showed that combining the spherically symmetric longrange interactions induced in a Rydberg-dressed BEC with infinite-range cavity-induced interactions establishes a versatile platform for studying the interplay between different interaction types and landscapes on the phases of quantum matter. Most strikingly, we point out a way towards realizing an amorphous solid in a robust and well-controlled system. The disorder in this phase is not imprinted from outside via some external potential or lattice but it is solely driven by quantum fluctuations and the interplay of the two interaction potentials. This dynamical, fluctuation induced formation of a superglass phase is closely related to the theoretically predicted phase transition from a liquid to a superglass after a temperature quench in helium-4 [48]. Our findings hint towards a realizable system to dynamically study phase transitions from a homogeneous or solid (CB phase) to a superglass by tuning the Rydberg interaction strength. The studied system is highly nonlinear and the formation of the intriguing phases presented in this paper involves the interplay between the BEC wave function  $\psi$  and the cavity mode  $\alpha$ . This makes easier the observation of Rydberg induced instabilities experimentally because the nonlinear coupling of atomic density fluctuations to the cavity mode facilitates the softening of the Rydberg roton. The formation of a density ordered pattern, i.e.,the dynamic minimization of the energy functional in Eq. (7), ultimately resembles an optimization problem with some given boundary conditions prescribed by the two interaction potentials. Hence, the fundamental physics presented here could open a way towards solving particular optimization problems by prescribing interaction potentials tailored to the problem at hand.

Our paper lays the groundwork for a variety of further studies combining long-range interacting systems theoretically as well as experimentally. Note that, in general, glasses have peculiar dynamic properties (diverging viscosity, etc.) and our findings open up a way to study the dynamics of a superglass phase in more detail. The research avenue outlined here is fostered by the new experimental and theoretical opportunities opening up in recently established experimental setups all over the world. Our proposed setup should be realizable in state-of-the-art cavity QED setups. In particular, the realization of the glassy phase where the parameters are favorable for experiments could readily be realized. However, the setup presented here is not the only system which is expected to exhibit such intriguing properties. Other promising avenues are combining other systems exhibiting light-induced instabilities in free space [32,62-67] with Rydberg dressing or long-range dipole interactions. More control over a wide range of realizable density patterns is expected if one assumes even more complex cavity-induced interaction potentials or Rydberg interactions. This can be achieved by changing to more complex cavity geometries such as multimode resonators [68–70] or dressing to spherically asymmetric Rydberg *p* states [71,72]. From a quantum optical viewpoint the dynamic transverse coupling of Rydberg atoms to a cavity could result in a highly nonlinear mechanism to enhance the achievable nonlinearities with state-of-the-art setups. The platform presented in this paper could also be extended to include spin degrees of freedom and serve as a viable tool to gain deeper understanding of spin glasses or even spin liquids [17,73].

While this paper focused on highlighting the remarkable features of this system and their intriguing consequences, several directions remain open for further research. One open and exciting question is the connection of the formation of the glassy phase to Anderson localization or even manybody localization. Also, the role of beyond mean-field effects and temperature needs further investigation. In this regard, also the role and potential breakdown of superfluidity in certain parameter regimes should be elucidated. To answer these questions, alternative theoretical techniques, which go beyond the scope of the present paper, have to be developed and applied [74–77]. In any case, the results presented in this paper open up exciting avenues in the growing research field of hybrid quantum systems with long-range interactions.

### ACKNOWLEDGMENTS

We would like to thank H. Ritsch for fruitful discussions. S.F.Y. would like to acknowledge funding by the AFOSR (applications of dense atomic media), the NSF (theory of dense atomic media), and the U.S. Department of Energy (structure of two-dimensional atomic media). S.O. is supported by a postdoctoral fellowship of the Max Planck Harvard Research Center for Quantum Optics. V.W. acknowledges support from the NSF through a grant for the Institute for Theoretical Atomic, Molecular, and Optical Physics at Harvard University and the Smithsonian Astrophysical Observatory. The numerical simulations were performed with the open-source framework QUANTUMOPTICS.JL [78].

## APPENDIX A: DETAILED MODEL DERIVATION

In the following we provide a concise derivation of the model presented in Sec. II. For a more detailed discussion of the underlying physics we refer to Refs. [54,79]. The full many-body Hamiltonian for the considered system can be written as the sum of five Hamiltonians  $H = H_a + H_{a-c} + H_c + H_{\text{int}}^{2-b} + H_{\text{int}}^{\text{Ryd}}$  with

$$H_{a} = \int d\mathbf{r} \Psi^{\dagger}(\mathbf{r}) \left[ -\frac{\hbar^{2} \nabla^{2}}{2m} + \hbar U_{p} \cos^{2}(k_{c}y) \right] \Psi(\mathbf{r}), \quad (A1a)$$

$$H_{a-c} = \int d\mathbf{r} \Psi^{\dagger}(\mathbf{r}) \left[ \hbar U_{0} \cos^{2}(k_{c}x) a^{\dagger} a + \hbar \eta \cos(k_{c}x) \cos(k_{c}y) (a + a^{\dagger}) \right] \Psi(\mathbf{r}), \quad (A1b)$$

$$H_c = -\hbar \Delta_c a^{\dagger} a, \tag{A1c}$$

$$H_{\text{int}}^{2-\text{b.}} = \frac{g}{2} \int d\mathbf{r} \Psi^{\dagger}(\mathbf{r}) \Psi^{\dagger}(\mathbf{r}) \Psi(\mathbf{r}) \Psi(\mathbf{r}), \tag{A1d}$$

$$H_{\text{int}}^{\text{Ryd}} = \iint d\mathbf{r} d\mathbf{r}' \Psi^{\dagger}(\mathbf{r}) \Psi^{\dagger}(\mathbf{r}') \frac{\tilde{C}_{6}}{R_{c}^{6} + |\mathbf{r} - \mathbf{r}'|^{6}} \Psi(\mathbf{r}') \Psi(\mathbf{r}). \tag{A1e}$$

Here,  $\Psi (\Psi^{\dagger})$  are annihilation (creation) operators of bosonic ground-state atoms, i.e.,  $[\Psi(\mathbf{r}), \Psi^{\dagger}(\mathbf{r}')] = \delta(\mathbf{r} - \mathbf{r}')$ , and  $a(a^{\dagger})$ are annihilation (creation) operators of the photonic cavity mode fulfilling  $[a, a^{\dagger}] = 1$ .  $U_p := \Omega_p^2/\Delta_p$  is the potential depth of the lattice generated by the two interfering pump beams and  $U_0 := \mathcal{G}_p^2/\Delta_p$  is the depth of the optical potential generated by photon scattering from the atomic density distribution inside the cavity. The effective cavity pump strength is given as  $\eta := \Omega_p \mathcal{G}_p / \Delta_p$  and  $k_c = 2\pi / \lambda_c$  denotes the wave number of the cavity mode. The Hamiltonian in Eq. (A1d) takes into account local two-body interactions between atoms and is omitted throughout this paper. This is a reasonable assumption since this interaction strength can be tuned to be small via, e.g.,a Feshbach resonance such that cavity and Rydberg induced long-range interactions dominate the dynamics [54,80]. The dynamics of the hybrid atom-cavity system is governed by the Heisenberg-Langevin equations  $i\hbar \partial_t \Psi(\mathbf{r}, t) = [\Psi(\mathbf{r}, t), H]$  and  $i\hbar \partial_t a(t) =$  $[a(t), H] - i\hbar\kappa a(t)$  where the decay of the cavity mode at a rate  $\kappa$  is included. Calculating these equations of motion and performing a mean-field approximation via  $\Psi(\mathbf{r},t) \rightarrow$  $\langle \Psi(\mathbf{r},t) \rangle := \psi(\mathbf{r},t)$  and  $a(t) \to \langle a(t) \rangle := \alpha(t)$  results in the two coupled c-number equations for the BEC order parameter  $\psi(\mathbf{r},t)$  and the cavity mode amplitude  $\alpha(t)$  given in Eq. (2) of the main text.

To adiabatically eliminate the cavity mode we calculate the equation of motion for the field operator a and solve for its steady state ( $\partial_t a = 0$ ). This results in

$$a_{\rm SS} = \frac{\eta \int d\mathbf{r} \Psi^{\dagger}(\mathbf{r}, t) \cos(k_c x) \cos(k_c y) \Psi(\mathbf{r}, t)}{\left[\Delta_c - U_0 \int d\mathbf{r} \Psi^{\dagger}(\mathbf{r}, t) \cos^2(k_c x) \Psi(\mathbf{r}, t)\right] + i\kappa}.$$
(A2)

Apart from the fundamental cavity parameters  $\eta$ ,  $\Delta_c$ , and  $\kappa$  the steady-state value for the cavity mode is determined by the two quantities

$$\Theta[\Psi(\mathbf{r},t)] := \int d\mathbf{r} \Psi^{\dagger}(\mathbf{r},t) \cos(k_c x) \cos(k_c y) \Psi(\mathbf{r},t), \quad (A3)$$

$$\mathcal{B}[\Psi(\mathbf{r},t)] := \int d\mathbf{r} \Psi^{\dagger}(\mathbf{r},t) \cos^{2}(k_{c}x) \Psi(\mathbf{r},t). \tag{A4}$$

These two quantities obviously depend on the BEC state which exhibits the nontrivial coupling between the cavity mode and the BEC. While  $\mathcal{B}$  only acts as an effective shift of the cavity resonance frequency that comes into play as soon as  $a_{\rm SS} \neq 0$ ,  $\Theta$  is the crucial parameter when it comes to understanding the cavity self-ordering phase transition. The cavity mode is nonzero if  $\Theta \neq 0$ . Hence this parameter is crucial for the instability described in the main text. To simplify the model we replace  $\mathcal{B}$  with its value for the homogeneous condensate  $\mathcal{B} = N/2$  while keeping the full functional dependence of  $\Theta$ . To eliminate the cavity field we plug the resultant steady-state solution into the many-body Hamiltonian. Since

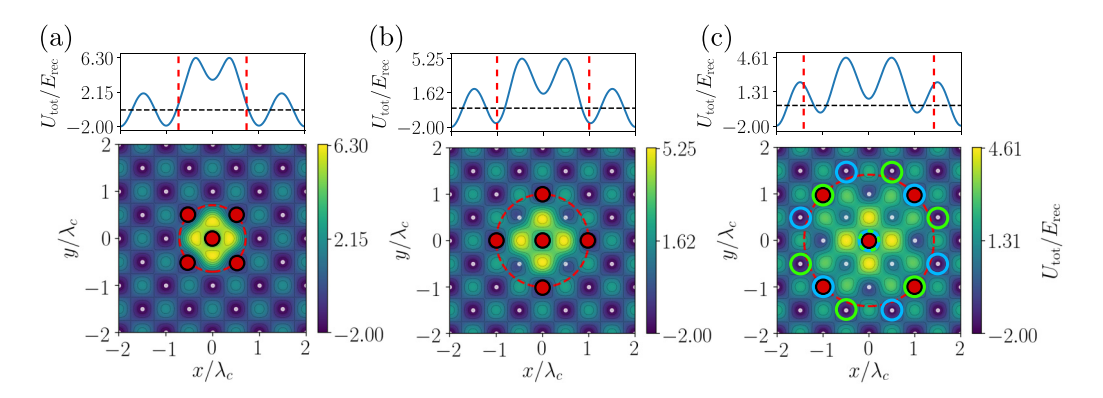


FIG. 9. Exemplary total interaction potentials from Eq. (B1) for the three cases treated throughout this paper. (a) Case (i),  $\eta = 1.0\eta_{crit}$  and  $\tilde{C}_6 = 0.1E_{rec}$ . (b) Case (ii),  $\eta = 1.0\eta_{crit}$  and  $\tilde{C}_6 = 0.5E_{rec}$ . (c) Case (iii),  $\eta = 1.0\eta_{crit}$  and  $\tilde{C}_6 = 3.0E_{rec}$ . The red dashed lines indicate the length scale imposed by the Rydberg roton. In panels (a) and (b) the red dots mark the first potential minima fulfilling the length scale restrictions imposed via the soft-core interaction potential. In panel (c) the light green and blue circles mark additional configurations fulfilling this restriction. This gives rise to a larger number of potential self-consistent ground states ultimately leading to the glassy behavior discussed in the main text. The dashed red lines indicate the length scale imposed by the Rydberg interaction potential for the respective cases.

we are solely interested in a model capturing the dynamic instability which is governed by terms  $\propto \cos(k_c x) \cos(k_c y)$ 

(see argument above) we keep only these terms. This results in the effective interaction Hamiltonian

$$H_{\text{int}}^{\text{cav}} = \hbar \mathcal{I} \iint d\mathbf{r} d\mathbf{r}' \Psi^{\dagger}(\mathbf{r}) \Psi^{\dagger}(\mathbf{r}') \cos(k_c x) \cos(k_c x') \cos(k_c y) \cos(k_c y') \Psi(\mathbf{r}') \Psi(\mathbf{r})$$
(A5)

where we used the symmetry of the cosine function in the second line and introduced the cavity induced interaction strength as

$$\mathcal{I} = \frac{\eta^2 (\Delta_c - NU_0/2)}{(\Delta_c - NU_0/2)^2 + \kappa^2}.$$
 (A6)

The many-body Hamiltonian for the BEC then reduces to  $\tilde{H} = -\int d\mathbf{r} \Psi^{\dagger}(\mathbf{r}) \frac{\hbar^2 \nabla^2}{2m} \Psi(\mathbf{r}) + H_{\rm int}^{\rm cav} + H_{\rm int}^{\rm Ryd}$ . The mean-field equation of motion given in Eq. (3) of the main text is found by calculating the Heisenberg equation of motion for  $\Psi(\mathbf{r},t)$  and again performing the mean-field approximation.

Note that in both GPEs presented in the main text [Eqs. (2a) and (3)] we neglected the potential term  $\propto \cos^2(k_c y)$ , which arises due to interference of the pump beams [see Eq. (A1a)]. This term is irrelevant for understanding the collective instabilities and the main fundamental results presented in this paper also hold if this term is included as we checked by including it in the numerics. However, neglecting this term facilitates the interpretation of the results and provides a method to understand the fundamental physics from an intuitive semianalytical standpoint as it is outlined in Sec. III of the main text. In fact, the interference between the two pump beams could even be suppressed in real experimental setups. This can either be achieved by choosing a large enough frequency difference between the two pump beams or by using two counterpropagating beams with orthogonal polarization. In this case, the model in Eq. (2) becomes exact.

## APPENDIX B: VARIATIONAL ALGORITHM

To find the self-consistent ground state in Sec. IV we employ a variational algorithm. Here we discuss this algorithm

in more detail. In particular, we focus on our choice of initial conditions and argue why the chosen initial conditions are good guesses for the final ground states. In Fig. 9, exemplary plots for the total interaction potential

$$U_{\text{tot}}(\mathbf{r}, \mathbf{r}') = U_{\text{cav}}(\mathbf{r}, \mathbf{r}') + U_{\text{Rvd}}(\mathbf{r}, \mathbf{r}'), \tag{B1}$$

defined as the sum of the two individual interaction potentials given in Eqs. (1) and (4), are shown. These potentials provide a good intuition about the anticipated ground states. Hence, we use these potentials as a guideline to define the initial conditions for the imaginary time evolution. We see that for the two special cases (i)  $(k_{cav} = k_{Ryd})$  and (ii)  $(k_{cav} = k_{Ryd})$  $k_{\rm Ryd}/\sqrt{2}$ ) the interaction potentials suggest a checkerboard pattern and a square lattice as a ground state which is indeed the self-consistent ground state in these particular cases [see Figs. 5(d) and 6(e)]. In addition, to those cases we choose the hcp lattice as an additional initial condition for all cases because this would be the ground state for a Rydberg-dressed BEC without cavity interactions [43]. From Fig. 9 we see that case (iii) is more complex than the previous two cases. In this case, the ground state could be a checkerboard lattice with larger period than in case (i) [see red dots in Fig. 9(c)] or one of the two lattice configurations indicated by the light green and blue circles in Fig. 9(c). Based on the above arguments it also becomes clear that only the cases where  $k_{\rm Rvd} < k_{\rm cav}$  result in modified results. If this condition is not fulfilled the length scale imposed by the Rydberg interaction potential is smaller than the cavity interaction potential which only modifies the corresponding interaction potential locally [see Fig. 9(a)].

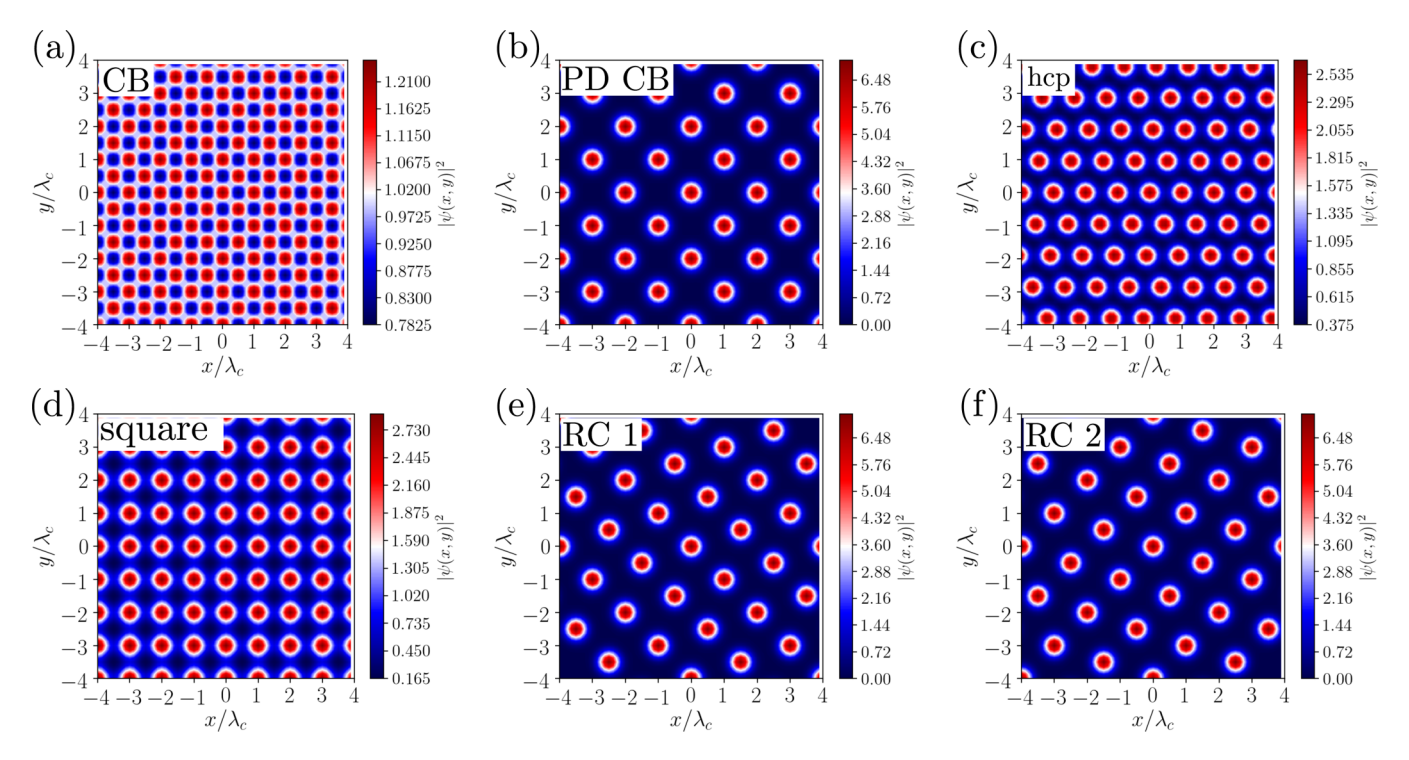


FIG. 10. The six nontrivial initial conditions (we refrain from showing the homogeneous state) based on the intuitive picture drawn in Fig. 9: (a) checkerboard pattern (CB), (b) period-doubled checkerboard pattern (PD CB), (c) hexagonal closed pack (hcp), (d) square lattice, (e) rotated chain version 1 (RC 1), and (f) rotated chain version 2 (RC 2).

Based on these intuitive arguments we generate the respective initial states  $\psi(\mathbf{r}) = \sum_i \phi_{\sigma}(\mathbf{r} - \mathbf{R}_i)$  by superimposing Gaussian wave functions  $\phi_{\sigma}(\mathbf{r}) = C \exp[-|\mathbf{r}|^2/(2\sigma^2)]$ . The resultant nontrivial initial conditions (we refrain from showing the homogeneous density) are shown in Fig. 10. We run

the variational algorithm discussed in Sec. IV for all these initial conditions for all cases (i)–(iii). We then compare the ground-state energies calculated via Eq. (7) and the resultant cavity mode amplitude to estimate whether the respective optimization problem is convex or not.

- H. J. Metcalf and P. van der Straten, Laser cooling and trapping of atoms, J. Opt. Soc. Am. B 20, 887 (2003).
- [2] S. Haroche and J.-M. Raimond, *Exploring the Quantum: Atoms, Cavities, and Photons* (Oxford University, New York, 2006)
- [3] I. Bloch, J. Dalibard, and W. Zwerger, Many-body physics with ultracold gases, Rev. Mod. Phys. **80**, 885 (2008).
- [4] A. Reiserer and G. Rempe, Cavity-based quantum networks with single atoms and optical photons, Rev. Mod. Phys. **87**, 1379 (2015).
- [5] C. Gross and I. Bloch, Quantum simulations with ultracold atoms in optical lattices, Science 357, 995 (2017).
- [6] A. Browaeys and T. Lahaye, Many-body physics with individually controlled Rydberg atoms, Nat. Phys. 16, 132 (2020).
- [7] N. Defenu, T. Donner, T. Macrì, G. Pagano, S. Ruffo, and A. Trombettoni, Long-range interacting quantum systems, arXiv:2109.01063.
- [8] A. Griesmaier, J. Werner, S. Hensler, J. Stuhler, and T. Pfau, Bose-Einstein Condensation of Chromium, Phys. Rev. Lett. 94, 160401 (2005).
- [9] M. Lu, N. Q. Burdick, S. H. Youn, and B. L. Lev, Strongly Dipolar Bose-Einstein Condensate of Dysprosium, Phys. Rev. Lett. 107, 190401 (2011).

- [10] K. Aikawa, A. Frisch, M. Mark, S. Baier, A. Rietzler, R. Grimm, and F. Ferlaino, Bose-Einstein Condensation of Erbium, Phys. Rev. Lett. 108, 210401 (2012).
- [11] M. A. Norcia and F. Ferlaino, New opportunites for interactions and control with ultracold lanthanides, arXiv:2108.04491.
- [12] H. Ritsch, P. Domokos, F. Brennecke, and T. Esslinger, Cold atoms in cavity-generated dynamical optical potentials, Rev. Mod. Phys. 85, 553 (2013).
- [13] F. Mivehvar, F. Piazza, T. Donner, and H. Ritsch, Cavity QED with quantum gases: New paradigms in many-body physics, Adv. Phys. **70**, 1 (2021).
- [14] A. Periwal, E. S. Cooper, P. Kunkel, J. F. Wienand, E. J. Davis, and M. Schleier-Smith, Programmable interactions and emergent geometry in an array of atomic clouds, Nature 600, 630 (2021).
- [15] S. Ebadi, T. T. Wang, H. Levine, A. Keesling, G. Semeghini, A. Omran, D. Bluvstein, R. Samajdar, H. Pichler, W. W. Ho, S. Choi, S. Sachdev, M. Greiner, V. Vuletić, and M. D. Lukin, Quantum phases of matter on a 256-atom programmable quantum simulator, Nature (London) 595, 227 (2021).
- [16] P. Scholl, M. Schuler, H. J. Williams, A. A. Eberharter, D. Barredo, K.-N. Schymik, V. Lienhard, L.-P. Henry, T. C. Lang, T. Lahaye, A. M. Läuchli, and A. Browaeys, Quantum simula-

- tion of 2D antiferromagnets with hundreds of Rydberg atoms, Nature (London) **595**, 233 (2021).
- [17] G. Semeghini, H. Levine, A. Keesling, S. Ebadi, T. T. Wang, D. Bluvstein, R. Verresen, H. Pichler, M. Kalinowski, R. Samajdar, A. Omran, S. Sachdev, A. Vishwanath, M. Greiner, V. Vuletic, and M. D. Lukin, Probing topological spin liquids on a programmable quantum simulator, Science 374, 1242 (2021).
- [18] M. Greiner, O. Mandel, T. Esslinger, T. W. Hänsch, and I. Bloch, Quantum phase transition from a superfluid to a Mott insulator in a gas of ultracold atoms, Nature (London) 415, 39 (2002).
- [19] J. Léonard, A. Morales, P. Zupancic, T. Esslinger, and T. Donner, Supersolid formation in a quantum gas breaking a continuous translational symmetry, Nature (London) 543, 87 (2017).
- [20] J.-R. Li, J. Lee, W. Huang, S. Burchesky, B. Shteynas, F. C. Top, A. O. Jamison, and W. Ketterle, A stripe phase with supersolid properties in spin-orbit-coupled Bose-Einstein condensates, Nature (London) 543, 91 (2017).
- [21] L. Tanzi, E. Lucioni, F. Famà, J. Catani, A. Fioretti, C. Gabbanini, R. N. Bisset, L. Santos, and G. Modugno, Observation of a Dipolar Quantum Gas with Metastable Supersolid Properties, Phys. Rev. Lett. 122, 130405 (2019).
- [22] F. Böttcher, J.-N. Schmidt, M. Wenzel, J. Hertkorn, M. Guo, T. Langen, and T. Pfau, Transient Supersolid Properties in an Array of Dipolar Quantum Droplets, Phys. Rev. X 9, 011051 (2019).
- [23] L. Chomaz, D. Petter, P. Ilzhöfer, G. Natale, A. Trautmann, C. Politi, G. Durastante, R. M. W. van Bijnen, A. Patscheider, M. Sohmen, M. J. Mark, and F. Ferlaino, Long-Lived and Transient Supersolid Behaviors in Dipolar Quantum Gases, Phys. Rev. X 9, 021012 (2019).
- [24] S. C. Schuster, P. Wolf, S. Ostermann, S. Slama, and C. Zimmermann, Supersolid Properties of a Bose-Einstein Condensate in a Ring Resonator, Phys. Rev. Lett. 124, 143602 (2020).
- [25] M. A. Norcia, C. Politi, L. Klaus, E. Poli, M. Sohmen, M. J. Mark, R. N. Bisset, L. Santos, and F. Ferlaino, Two-dimensional supersolidity in a dipolar quantum gas, Nature (London) 596, 357 (2021).
- [26] T. Bland, E. Poli, C. Politi, L. Klaus, M. A. Norcia, F. Ferlaino, L. Santos, and R. N. Bisset, Two-dimensional supersolidity in a circular trap, arXiv:2107.06680.
- [27] J. Zeiher, J.-y. Choi, A. Rubio-Abadal, T. Pohl, R. van Bijnen, I. Bloch, and C. Gross, Coherent Many-Body Spin Dynamics in a Long-Range Interacting Ising Chain, Phys. Rev. X 7, 041063 (2017).
- [28] R. Samajdar, W. W. Ho, H. Pichler, M. D. Lukin, and S. Sachdev, Complex Density Wave Orders and Quantum Phase Transitions in a Model of Square-Lattice Rydberg Atom Arrays, Phys. Rev. Lett. 124, 103601 (2020).
- [29] S. Gopalakrishnan, B. L. Lev, and P. M. Goldbart, Frustration and Glassiness in Spin Models with Cavity-Mediated Interactions, Phys. Rev. Lett. 107, 277201 (2011).
- [30] A. Angelone, F. Mezzacapo, and G. Pupillo, Superglass Phase of Interaction-Blockaded Gases on a Triangular Lattice, Phys. Rev. Lett. **116**, 135303 (2016).
- [31] J. Hertkorn, J.-N. Schmidt, M. Guo, F. Böttcher, K. S. H. Ng, S. D. Graham, P. Uerlings, T. Langen, M. Zwierlein, and T. Pfau, Pattern formation in quantum ferrofluids: From

- supersolids to superglasses, Phys. Rev. Research 3, 033125 (2021).
- [32] G. Baio, G. R. M. Robb, A. M. Yao, G.-L. Oppo, and T. Ackemann, Multiple Self-Organized Phases and Spatial Solitons in Cold Atoms Mediated by Optical Feedback, Phys. Rev. Lett. 126, 203201 (2021).
- [33] J. Smith, A. Lee, P. Richerme, B. Neyenhuis, P. W. Hess, P. Hauke, M. Heyl, D. A. Huse, and C. Monroe, Many-body localization in a quantum simulator with programmable random disorder, Nat. Phys. 12, 907 (2016).
- [34] J.-y. Choi, S. Hild, J. Zeiher, P. Schauß, A. Rubio-Abadal, T. Yefsah, V. Khemani, D. A. Huse, I. Bloch, and C. Gross, Exploring the many-body localization transition in two dimensions, Science 352, 1547 (2016).
- [35] Y. Zhou, K. Kanoda, and T.-K. Ng, Quantum spin liquid states, Rev. Mod. Phys. 89, 025003 (2017).
- [36] K. Viebahn, M. Sbroscia, E. Carter, J.-C. Yu, and U. Schneider, Matter-Wave Diffraction from a Quasicrystalline Optical Lattice, Phys. Rev. Lett. 122, 110404 (2019).
- [37] F. Mivehvar, H. Ritsch, and F. Piazza, Emergent Quasicrystalline Symmetry in Light-Induced Quantum Phase Transitions, Phys. Rev. Lett. **123**, 210604 (2019).
- [38] A. Mendoza-Coto, R. Turcati, V. Zampronio, R. Díaz-Méndez, T. Macrì, and F. Cinti, Exploring quantum quasicrystal patterns: a variational study, arXiv:2110.12299.
- [39] A. Grankin, E. Brion, E. Bimbard, R. Boddeda, I. Usmani, A. Ourjoumtsev, and P. Grangier, Quantum-optical nonlinearities induced by Rydberg-Rydberg interactions: A perturbative approach, Phys. Rev. A 92, 043841 (2015).
- [40] R. Boddeda, I. Usmani, E. Bimbard, A. Grankin, A. Ourjoumtsev, E. Brion, and P. Grangier, Rydberg-induced optical nonlinearities from a cold atomic ensemble trapped inside a cavity, J. Phys. B 49, 084005 (2016).
- [41] J. Gelhausen, M. Buchhold, A. Rosch, and P. Strack, Quantum-optical magnets with competing short- and long-range interactions: Rydberg-dressed spin lattice in an optical cavity, SciPost Phys. 1, 004 (2016).
- [42] P. Strack and S. Sachdev, Dicke Quantum Spin Glass of Atoms and Photons, Phys. Rev. Lett. 107, 277202 (2011).
- [43] N. Henkel, F. Cinti, P. Jain, G. Pupillo, and T. Pohl, Supersolid Vortex Crystals in Rydberg-Dressed Bose-Einstein Condensates, Phys. Rev. Lett. **108**, 265301 (2012).
- [44] R. Mottl, F. Brennecke, K. Baumann, R. Landig, T. Donner, and T. Esslinger, Roton-Type Mode Softening in a Quantum Gas with Cavity-Mediated Long-Range Interactions, Science 336, 1570 (2012).
- [45] K. Barkan, M. Engel, and R. Lifshitz, Controlled Self-Assembly of Periodic and Aperiodic Cluster Crystals, Phys. Rev. Lett. 113, 098304 (2014).
- [46] B. R. de Abreu, F. Cinti, and T. Macrì, Superstripes and quasicrystals in bosonic systems with hard-soft corona interactions, arXiv:2009.10203.
- [47] G. Pupillo, P. Ziherl, and F. Cinti, Quantum cluster quasicrystals, Phys. Rev. B 101, 134522 (2020).
- [48] M. Boninsegni, N. Prokof'ev, and B. Svistunov, Superglass Phase of <sup>4</sup>He, Phys. Rev. Lett. 96, 105301 (2006).
- [49] G. Biroli, C. Chamon, and F. Zamponi, Theory of the superglass phase, Phys. Rev. B 78, 224306 (2008).

- [50] K.-M. Tam, S. Geraedts, S. Inglis, M. J. P. Gingras, and R. G. Melko, Superglass Phase of Interacting Bosons, Phys. Rev. Lett. 104, 215301 (2010).
- [51] A. Angelone, T. Ying, F. Mezzacapo, G. Masella, M. Dalmonte, and G. Pupillo, Nonequilibrium scenarios in cluster-forming quantum lattice models, Phys. Rev. A 101, 063603 (2020).
- [52] J. E. Johnson and S. L. Rolston, Interactions between Rydbergdressed atoms, Phys. Rev. A 82, 033412 (2010).
- [53] J. Honer, H. Weimer, T. Pfau, and H. P. Büchler, Collective Many-Body Interaction in Rydberg Dressed Atoms, Phys. Rev. Lett. 105, 160404 (2010).
- [54] N. Henkel, R. Nath, and T. Pohl, Three-Dimensional Roton Excitations and Supersolid Formation in Rydberg-Excited Bose-Einstein Condensates, Phys. Rev. Lett. 104, 195302 (2010).
- [55] F. Maucher, N. Henkel, M. Saffman, W. Królikowski, S. Skupin, and T. Pohl, Rydberg-Induced Solitons: Three-Dimensional Self-Trapping of Matter Waves, Phys. Rev. Lett. 106, 170401 (2011).
- [56] J. B. Balewski, A. T. Krupp, A. Gaj, S. Hofferberth, R. Löw, and T. Pfau, Rydberg dressing: Understanding of collective manybody effects and implications for experiments, New J. Phys. 16, 063012 (2014).
- [57] D. Nagy, G. Szirmai, and P. Domokos, Self-organization of a Bose-Einstein condensate in an optical cavity, Eur. Phys. J. D 48, 127 (2008).
- [58] C.-H. Hsueh, T.-C. Lin, T.-L. Horng, and W. C. Wu, Quantum crystals in a trapped Rydberg-dressed Bose-Einstein condensate, Phys. Rev. A **86**, 013619 (2012).
- [59] L. Landau, Theory of the Superfluidity of Helium II, Phys. Rev. 60, 356 (1941).
- [60] L. Pitaevskii and S. Stringari, Bose-Einstein Condensation and Superfluidity, Vol. 164 (Oxford University, New York, 2016).
- [61] K. Baumann, R. Mottl, F. Brennecke, and T. Esslinger, Exploring Symmetry Breaking at the Dicke Quantum Phase Transition, Phys. Rev. Lett. **107**, 140402 (2011).
- [62] S. Ostermann, F. Piazza, and H. Ritsch, Spontaneous Crystallization of Light and Ultracold Atoms, Phys. Rev. X 6, 021026 (2016).
- [63] W. J. Firth, I. Krešić, G. Labeyrie, A. Camara, and T. Ackemann, Thick-medium model of transverse pattern formation in optically excited cold two-level atoms with a feedback mirror, Phys. Rev. A 96, 053806 (2017).
- [64] S. Ostermann, F. Piazza, and H. Ritsch, Probing and characterizing the growth of a crystal of ultracold bosons and light, New J. Phys. 19, 125002 (2017).
- [65] I. Dimitrova, W. Lunden, J. Amato-Grill, N. Jepsen, Y. Yu, M. Messer, T. Rigaldo, G. Puentes, D. Weld, and W. Ketterle, Observation of two-beam collective scattering phenomena in a Bose-Einstein condensate, Phys. Rev. A 96, 051603(R) (2017).

- [66] Y.-C. Zhang, V. Walther, and T. Pohl, Long-Range Interactions and Symmetry Breaking in Quantum Gases through Optical Feedback, Phys. Rev. Lett. 121, 073604 (2018).
- [67] Y.-C. Zhang, V. Walther, and T. Pohl, Self-bound droplet clusters in laser-driven Bose-Einstein condensates, Phys. Rev. A 103, 023308 (2021).
- [68] T. Keller, V. Torggler, S. B. Jäger, S. Schütz, H. Ritsch, and G. Morigi, Quenches across the self-organization transition in multimode cavities, New J. Phys. 20, 025004 (2018).
- [69] Y. Guo, R. M. Kroeze, V. D. Vaidya, J. Keeling, and B. L. Lev, Sign-Changing Photon-Mediated Atom Interactions in Multimode Cavity Quantum Electrodynamics, Phys. Rev. Lett. 122, 193601 (2019).
- [70] Y. Guo, V. D. Vaidya, R. M. Kroeze, R. A. Lunney, B. L. Lev, and J. Keeling, Emergent and broken symmetries of atomic self-organization arising from Gouy phase shifts in multimode cavity QED, Phys. Rev. A 99, 053818 (2019).
- [71] A. W. Glaetzle, M. Dalmonte, R. Nath, I. Rousochatzakis, R. Moessner, and P. Zoller, Quantum Spin-Ice and Dimer Models with Rydberg Atoms, Phys. Rev. X 4, 041037 (2014).
- [72] A. W. Glaetzle, M. Dalmonte, R. Nath, C. Gross, I. Bloch, and P. Zoller, Designing Frustrated Quantum Magnets with Laser-Dressed Rydberg Atoms, Phys. Rev. Lett. 114, 173002 (2015).
- [73] D. Sherrington and S. Kirkpatrick, Solvable Model of a Spin-Glass, Phys. Rev. Lett. 35, 1792 (1975).
- [74] M. Boninsegni, N. Prokof'ev, and B. Svistunov, Worm Algorithm for Continuous-Space Path Integral Monte Carlo Simulations, Phys. Rev. Lett. 96, 070601 (2006).
- [75] M. Boninsegni, N. V. Prokof'ev, and B. V. Svistunov, Worm algorithm and diagrammatic Monte Carlo: A new approach to continuous-space path integral Monte Carlo simulations, Phys. Rev. E 74, 036701 (2006).
- [76] R. Lin, L. Papariello, P. Molignini, R. Chitra, and A. U. J. Lode, Superfluid-Mott-insulator transition of ultracold superradiant bosons in a cavity, Phys. Rev. A 100, 013611 (2019).
- [77] R. Lin, C. Georges, J. Klinder, P. Molignini, M. Büttner, A. U. J. Lode, R. Chitra, A. Hemmerich, and H. Keßler, Mott transition in a cavity-boson system: A quantitative comparison between theory and experiment, SciPost Phys. 11, 030 (2021).
- [78] S. Krämer, D. Plankensteiner, L. Ostermann, and H. Ritsch, QuantumOptics.jl: A Julia framework for simulating open quantum systems, Comput. Phys. Commun. 227, 109 (2018).
- [79] C. Maschler, I. B. Mekhov, and H. Ritsch, Ultracold atoms in optical lattices generated by quantized light fields, Eur. Phys. J. D 46, 545 (2008).
- [80] F. Brennecke, R. Mottl, K. Baumann, R. Landig, T. Donner, and T. Esslinger, Real-time observation of fluctuations at the driven-dissipative Dicke phase transition, Proc. Natl. Acad. Sci. USA 110, 11763 (2013).